

Searching Ternary Oxides and Chalcogenides as Positive Electrodes for Calcium Batteries

Wang Lu, Juefan Wang, Gopalakrishnan Sai Gautam,* and Pieremanuele Canepa*



Cite This: *Chem. Mater.* 2021, 33, 5809–5821



Read Online

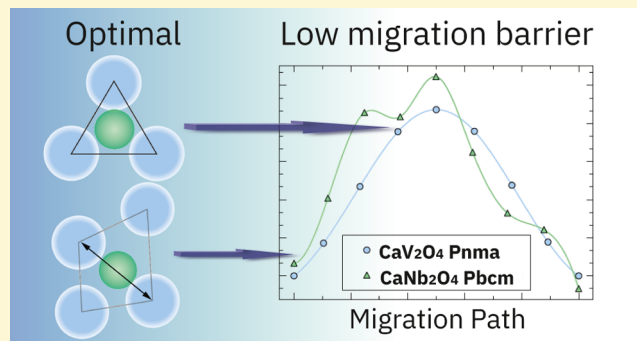
ACCESS |

Metrics & More

Article Recommendations

Supporting Information

ABSTRACT: The identification of alternatives to the lithium-ion battery architecture remains a crucial priority in the diversification of energy storage technologies. Accompanied by the low reduction potential of Ca^{2+}/Ca , -2.87 V vs standard hydrogen electrode, metal-anode-based rechargeable calcium (Ca) batteries appear competitive in terms of energy densities. However, the development of Ca batteries lacks high-energy-density intercalation cathode materials. Using first-principles methodologies, we screen a large chemical space for potential Ca -based cathode chemistries, with composition of $\text{Ca}_i\text{TM}_j\text{Z}_k$, where TM is a first- or second-row transition metal and Z is oxygen, sulfur, selenium, or tellurium. Ten materials are selected, and their Ca intercalation properties are investigated. We identify two previously unreported promising electrode compositions: the post-spinel CaV_2O_4 and the layered CaNb_2O_4 , with Ca migration barriers of ~ 654 and ~ 785 meV, respectively. We analyze the geometrical features of the Ca migration pathways across the 10 materials studied and provide an updated set of design rules for the identification of good ionic conductors, especially with large mobile cations.



1. INTRODUCTION

The lithium (Li)-ion battery technology is well established and has been commercialized for the past three decades, with important but incremental improvements in terms of its energy density, reliability, and safety.^{1–7} However, the energy density prerequisites to drive stationary energy storage devices and electric vehicles are quickly exceeding the limits of what can be achieved by commercial Li-ion batteries.⁸ Finding suitable alternatives to the rocking-chair Li-ion battery is a crucial priority in the diversification and modernization of energy storage technologies. Rechargeable energy storage devices based on multivalent ions, e.g., magnesium Mg^{2+} , calcium Ca^{2+} , and zinc Zn^{2+} , have emerged as interesting alternatives to their Li-ion analogues.^{9,10} In particular, metal-anode-based rechargeable Ca batteries appear competitive in terms of energy densities, given the high gravimetric capacity, ~ 2205 mAh/g, the low standard reduction potential of Ca^{2+}/Ca , -2.87 V vs standard hydrogen electrode (SHE), and the large volumetric capacity, ~ 2073 Ah/l.^{9–13}

While a Ca -based chemistry is promising in theory, a number of unresolved challenges stand out. First of all, the lack of practical electrolytes that can simultaneously tolerate the reducing environment of a Ca -metal anode and the oxidizing nature of a high-voltage (and high-capacity) Ca -intercalation cathode.^{14–31} Another significant challenge is the identification of fast Ca^{2+} conductors that can act as reversible, high-voltage, and high-capacity intercalation cathodes, which is the focus of this work.^{32–34}

A reasonable figure of merit to identify potential Ca cathodes with high Ca^{2+} conductivity is represented by the migration barrier, E_m —the energy that Ca^{2+} must overcome during its migration between two identical crystallographic sites in an anion host framework. Rong et al.³² proposed values of ca. 525–650 meV as tolerable limits for E_m in electrodes, where the lower (upper) limit represents micron (nano)-sized electrode particles operating at room temperature and a rate of C/2. If the cathode particle sizes are decreased or the temperature of operation is increased or the rate of battery (dis)charge is decreased, the upper limit on E_m can be further increased.³³ For example, the upper limit on E_m can be increased up to ~ 895 meV if the cathode particles of size 10 nm are cycled at 333 K ($\sim 60^\circ\text{C}$) at a C/6 rate (6 h of charge/discharge).³³

Implementing the E_m criteria, Rong et al.³² investigated a number of close-packed frameworks predominantly used in Li-ion batteries, i.e., the spinel (Mn_2O_4), the layered (NiO_2), and the olivine (FePO_4) prototypes, respectively. Three design rules to facilitate the identification of fast multivalent conductors were discovered, based on the cation coordination environments and

Received: June 10, 2021

Revised: July 6, 2021

Published: July 16, 2021



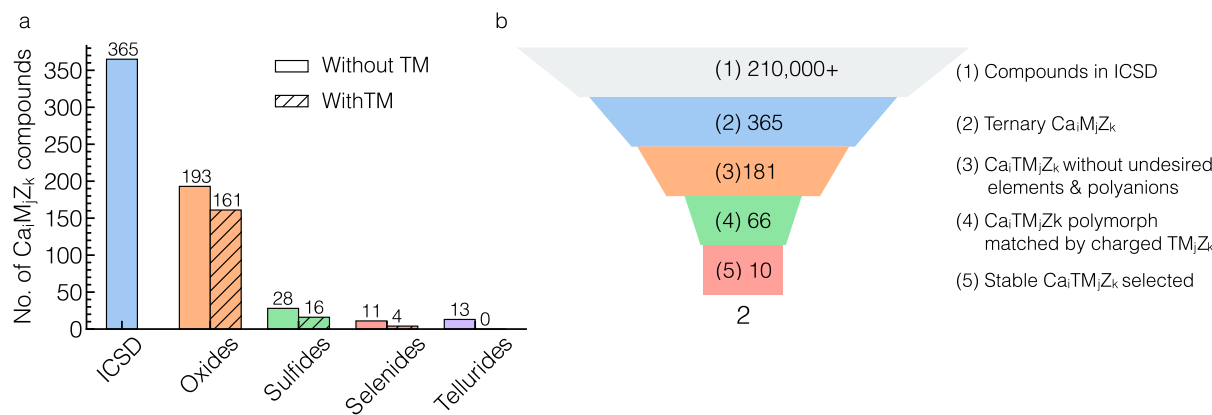


Figure 1. (a) Distribution of ternary $\text{Ca}_i\text{M}_j\text{Z}_k$ compounds, where $\text{Z} = \text{O}, \text{S}, \text{Se}$, or Te , and M is a non-Ca cation. Hatched bars indicate $\text{Ca}_i\text{TM}_j\text{Z}_k$ -like compounds with a transition metal (TM) of the d -block and Z any chalcogen element, i.e., O, S, Se, or Te. (b) Filtering procedure to identify ternary Ca-containing electrodes with the composition $\text{Ca}_i\text{TM}_j\text{Z}_k$, where TM is redox-active. The number in each colored panel identifies the number of accepted materials at each stage of the screening.

the volume per anion available in a host framework (see [Section 3](#) for a detailed description).^{32,35} Given the large values (>525 meV) of E_m estimated for Ca migration in layered and olivine frameworks, and the intrinsic instability of Ca-containing spinel frameworks, the authors concluded that these structures are unsuitable for Ca batteries.³²

Recently, Vaughney and co-workers reported reversible intercalation of 0.6 mol Ca^{2+} into NaSICON- $\text{NaV}_2(\text{PO}_4)_3$, equivalent to a capacity of ~ 81 mAh/g at 3.2 V vs Ca/Ca^{2+} ,³⁶ while similar experiments with olivine- FePO_4 yielded partially reversible Ca intercalation, with an initial capacity of ~ 72 mAh/g at ~ 2.9 V vs Ca/Ca^{2+} .³⁶ These experimental results on olivine- FePO_4 are in qualitative agreement with Rong et al.,³² who predicted a moderate Ca migration barrier (~ 580 meV) in the charged state of olivine- FePO_4 . Recently, the group of Kang could reversibly extract Ca^{2+} ions from $\text{Na}_{1.5}\text{VPO}_{4.8}\text{F}_{0.7}$ and reported a capacity of 87 mAh/g and 90% capacity retention over 500 cycles.³¹

Additional theoretical work^{32,37} revealed that E_m for Ca in $\delta\text{-V}_2\text{O}_5$ could be as low as ~ 200 meV. However, $\delta\text{-V}_2\text{O}_5$ is not the stable polymorph, with E_m for Ca being predicted to be prohibitively high (ca. 1700–1900 meV) in the stable $\alpha\text{-V}_2\text{O}_5$ polymorph.³⁷ Although Ca intercalation in $\alpha\text{-V}_2\text{O}_5$ has received significant attention,^{38–40} Verrelli et al.³⁹ confirmed the unsuitability of V_2O_5 as a cathode for Ca batteries owing to lack of robust Ca intercalation, chemically or electrochemically.

The search for potential Ca cathodes has progressed steadily in the recent past with a handful of research groups fully dedicated to the task. For example, the teams led by Palacín and Ponrouch have extensively investigated TiS_2 using different temperatures, electrolyte formulations, and observed reversible Ca intercalation (accompanied by solvent co-intercalation) from a $\text{Ca}(\text{TFSI})_2\text{:PC}$ electrolyte at moderate temperatures (~ 60 and 100 °C).^{41,42} The same teams have also reported the irreversible Ca extraction from $\text{Ca}_{0.89}\text{TaN}_2$.⁴³ Tirado and collaborators observed Ca intercalation from a nonaqueous electrolyte into the hydrated phase of layered $\alpha\text{-MoO}_3$,⁴⁴ and claimed a gravimetric capacity of ~ 100 mAh/g at a low voltage of ~ 1.3 V vs Ca/Ca^{2+} , with additional corroboration from computational models.

On the computational front, using density functional theory (DFT)^{45,46} Arroyo-de Dompablo et al. spearheaded the investigation (and discovery) of alternative Ca-intercalation chemistries, including oxide (i.e., CaMn_2O_4 , $\text{Ca}_2\text{Mn}_2\text{O}_5$,

CaMn_4O_8 , $\text{Ca}_2\text{Fe}_2\text{O}_5$, $\text{Ca}_4\text{Fe}_9\text{O}_{17}$, $\text{Ca}_3\text{Co}_4\text{O}_9$, and $\text{Ca}_3\text{Co}_2\text{O}_6$) and mixed anion (i.e., CaFeSO , CaCoSO , CaNiN , Ca_3MnN_3 , $\text{Ca}_2\text{Fe}(\text{Si}_2\text{O}_7)$, $\text{CaM}(\text{P}_2\text{O}_7)$ with $\text{M} = \text{V}, \text{Cr}, \text{Mn}$ Fe and Co, $\text{CaV}_2(\text{P}_2\text{O}_7)_2$, $\text{Ca}(\text{VO})_2(\text{PO}_4)_2$, and $\alpha\text{-VOPO}_4$) frameworks.^{47–52} For example, they reported a low Ca E_m of ~ 650 meV in $\alpha\text{-VOPO}_4$, along with the high theoretical gravimetric capacity (~ 312 mAh/g) and average (theoretical) intercalation voltage of ~ 2.8 V vs Ca/Ca^{2+} , making VOPO₄ a promising candidate for further experimental investigation.

Undoubtedly, the above experimental and theoretical studies have made sizeable progress toward the development of practical Ca-battery prototypes. However, a more streamlined theoretical (and experimental) effort can accelerate the search for cathodes with facile Ca^{2+} migration, thus facilitating the development of this promising energy storage platform. Here, we have used an efficient screening of Ca-containing ternary structures, utilizing a combination of structural information, characterization conditions, and theoretically predicted thermodynamic stability, and subsequently evaluated the battery properties of key candidates using DFT-based calculations to push forward the discovery of novel Ca cathodes. We focus on unveiling overlooked potential cathode chemistries with a general composition of $\text{Ca}_i\text{TM}_j\text{Z}_k$, where TM is a first- or second-row transition metal and Z is oxygen, sulfur, selenium, or tellurium. In the present work, we have not considered any low gravimetric capacity, mixed anion frameworks, or any halogen-based structures.

From our search, we propose two new promising candidates, namely, the post-spinel CaV_2O_4 and the layered CaNb_2O_4 . Specifically, the calculated E_m in both CaV_2O_4 (~ 654 meV) and CaNb_2O_4 (~ 785 meV) fulfill the criteria for Ca conductors with reasonable Ca^{2+} ion conductivity. As further validation of our proposed screening strategy, we rediscovered the Chevrel- Mo_6S_8 and CaMoO_3 compounds, which have already been studied both computationally and experimentally.^{44,48,53} Finally, we revisit and propose modifications to the design rules put forward by Rong et al. for good multivalent conductors,³² which can be further extended to discover novel conductors for Ca batteries and beyond.

2. RESULTS

2.1. Screening Procedure of $\text{Ca}_i\text{TM}_j\text{Z}_k$ Electrode Materials.

[Figure 1a](#) shows the distribution of Ca-containing

Table 1. Computed Characteristics of the 10 Discharged $\text{Ca}_i\text{TM}_j\text{Z}_k$ and Charged TM_jZ_k Compounds Resulting from our Screening^a

material	ICSD/MP	space group	mechanism	E^{hull}	CN	E_m	voltage	capacity	specific	cost
CaV_3O_7	2507	<i>Pnma</i>		2	7	2892		176		17.40 ^b
V_3O_7	mvc-13330	<i>Pnma</i>	T	51			3.34		587	
V_3O_7	mp-622640	<i>C2/c</i>	N	8			3.11		547	
$\text{Ca}_2\text{V}_2\text{O}_6$	237336	<i>Pnma</i>		0	7	3235		193		17.40 ^b
CaV_2O_6	this work ^e	$\text{Pnma} \rightarrow \text{Pmn}2_1$	T	95			2.96		571	
CaV_2O_6	21064	<i>C2/m</i>	N	0			2.46		474	
CaV_2O_4	164185	<i>Pnma</i>		0	8	654		260		17.40 ^b
V_2O_4	mp-777479	<i>Pnma</i>	T	26			2.40		624	
V_2O_4	10 141	<i>P4_2/mnm</i>	N	0			2.34		608	
CaNb_2O_4	88 779	<i>Pbcm</i>		0	6	785		185		30.20 ^c
Nb_2O_4	this work ^e	$\text{Pbcm} \rightarrow \text{Pmma}$	T	308			2.71		501	
Nb_2O_4	96	<i>I4_1/a</i>	N	0			1.78		329	
$\text{Ca}_5\text{Cu}_6\text{O}_{12}$	91 059	<i>P2_1/c</i>		28	6			139		8.75 ^d
$\text{Ca}_3\text{Cu}_6\text{O}_{12}$	this work ^e	$\text{P2}_1/\text{c} \rightarrow \text{P2}_1$	T	92			3.19		443	
$\text{Ca}_3\text{Cu}_6\text{O}_{12}$	mp-1540145	<i>I4_1/a</i>	N	0			2.83		393	
CaMoO_3	246 082	<i>P2_1/c</i>		0	8	2072		291		24.75 ^d
MoO_3	mp-18856	<i>P2_1/c</i>	T	0			2.77		806	
MoO_3	35 076	<i>Pnma</i>	N	39			2.76		803	
CaIrO_3	420 479	<i>Cmcm</i>	T	0	8	1219	3.29	191	629	193 000.00 ^d
IrO_3	mp-1097041	<i>Cmcm</i>		0						
CaRh_2O_4	170 597	<i>Pnma</i>		0	8	1110		173		860 000.00 ^d
Rh_2O_4	this work	<i>Pnma</i>	T	67			2.84		491	
Rh_2O_4	28 498	<i>P4_2/mnm</i>	N	0			2.63		455	
CaCu_2S_2	241 336	<i>P\bar{3}m1</i>		0	6	1622		232		8.75 ^d
Cu_2S_2	this work ^e	$\text{P}\bar{3}m1 \rightarrow \text{C}2/\text{m}$	T	108			2.17		503	
Cu_2S_2	63 328	<i>Cmcm</i>	N	0			1.95		452	
CaMo_6S_8	619 423	<i>R\bar{3}</i>	T	17	8		1.82	61	112	24.75 ^d
Mo_6S_8	86 788	<i>R\bar{3}</i>		66						
$\alpha\text{-CaV}_2\text{O}_5^f$	82 689	<i>Pmmm</i>	T	0	8	1869	3.13	241	757	17.40 ^b
V_2O_5	15 798	<i>Pmmm</i>		0						

^aThe ICSD or MP ID of each material is provided. E^{hull} , voltage, capacity (capacity), specific energy (specific) and cost of transition metal are reported in units of meV/atom, volts vs Ca/Ca^{2+} , mAh/g, Wh/kg, and \$/kg, respectively. Mechanism indicates whether Ca intercalation follows a topotactic (T) or a nontopotactic (N) mechanism. The average coordination number (CN) of Ca^{2+} and the computed E_m (in meV) in the discharged structures (i.e., dilute vacancy limit) are also reported. ^bVanadium price obtained from <https://www.vanadiumprice.com> and sold as V_2O_5 . ^cNiobium price obtained from <https://www.niobiumprice.com> and sold as Nb_2O_5 . ^dMetal prices obtained from <https://www.dailymetalprice.com/>. ^eUpon topotactic extraction of Ca^{2+} , the symmetry of the charged structure becomes different from the discharged structure. ^fConsidered as a calibration compound.

ternary compounds, with prototype formula $\text{Ca}_i\text{M}_j\text{Z}_k$, where M is a generic cation (and not necessarily an open-shell transition metal) and Z is the anion species, as obtained from the inorganic crystal structure database (ICSD).^{54,55} We excluded structures with non-Ca cations that can potentially exhibit electrochemical activity, such as Li, Na, Mg, Zn, K, Rb, and Cs, from the list of cations considered as M. In the remainder of this study, we will address as chalcogenides all compounds with formula $\text{Ca}_i\text{M}_j\text{Z}_k$, where Z can be O, S, Se, or Te. Of the more than 210 000 structures in ICSD, only 412 satisfy the compositional constraint of $\text{Ca}_i\text{M}_j\text{Z}_k$ with $Z = \text{O, S, Se, or Te}$. Furthermore, a significant portion of identified $\text{Ca}_i\text{M}_j\text{Z}_k$ constitutes unsurprisingly oxides^{56,57} (orange bars in Figure 1a), with a considerably lower number of other chalcogenides.

The hatched bars in Figure 1a represent $\text{Ca}_i\text{TM}_j\text{Z}_k$ compounds with a transition metal TM of the d-block and any chalcogen element Z, i.e., O, S, Se, or Te. Therefore, the hatched bars exclude mixed anion moieties, such as SiO_4^{4-} , PO_4^{3-} , etc. Figure 1b presents our search strategy to identify potential Ca conductors/electrodes, with chemical formula $\text{Ca}_i\text{TM}_j\text{Z}_k$. We utilized the combined information available in the ICSD (i.e., structures and characterization conditions),⁵⁵ and the Materials

Project (MP; thermodynamic stabilities)⁵⁸ to arrive at our candidates. The screening procedure, where we induce constraints on chemical composition, redox activity, charge balance, and thermodynamic stability, followed the steps:

1. Identification of $\text{Ca}_i\text{M}_j\text{Z}_k$ compounds in the ICSD. This initial screen could identify 412 chalcogenides $\text{Ca}_i\text{M}_j\text{Z}_k$ materials as shown in Figure 1a.
2. Selection of $\text{Ca}_i\text{TM}_j\text{Z}_k$ compounds with a transition metal TM of the d-block, where the TM must be a redox-active element. For example, even though Sc and Zn are d-block TMs, they are not known to be redox-active. As shown in Figure 1b, this important filter could further reduce our dataset to 181 $\text{Ca}_i\text{TM}_j\text{Z}_k$ candidates, of which only 161 are oxides, 16 are sulfides and 4 are selenides (see Figure 1b). Furthermore, all 13 telluride $\text{Ca}_i\text{M}_j\text{Z}_k$ compounds were entirely made by mixed anion species (e.g., TeO_6^{2-}) and are eliminated from our selection. In this step, we also eliminated all $\text{Ca}_i\text{TM}_j\text{Z}_k$ that were characterized under nonambient conditions.
3. Identification of discharged compositions $\text{Ca}_i\text{TM}_j\text{Z}_k$ which can be matched by charge-balanced decalcinated

compositions TM_jZ_k . As Ca is deintercalated from a $\text{Ca}_i\text{TM}_j\text{Z}_k$ either partially or fully, it is important that the TM species exhibits oxidation states that are physically plausible, hence ensuring charge neutrality of the deintercalated composition. For example, CaVO_3 is a well-known Ca-containing orthorhombic perovskite that satisfies the chemical formula of $\text{Ca}_i\text{TM}_j\text{Z}_k$ and contains an open-shell transition metal (i.e., V^{4+}). However, the fully charged version of CaVO_3 , namely, VO_3 , requires V to exhibit an oxidation state of 6+, which is not physical. Thus, CaVO_3 does not qualify as a candidate across this filter. Note that charge neutrality is one of the necessary, but not sufficient, conditions for thermodynamic stability. Hence, during this filtering process, we tried to identify possible charge-neutral deintercalated composition(s) for every $\text{Ca}_i\text{TM}_j\text{Z}_k$ considered. In particular, we checked the availability of ordered structures of both fully (TM_jZ_k) and partially ($\text{Ca}_{1-i}\text{TM}_j\text{Z}_k$) deintercalated compositions that were charge-neutral in the ICSD as well as Materials Project. Although any of the screened Ca chemistries may allow partial decalcination, we preferred fully charged structures in all possible cases, since that maximizes theoretical capacities. We only considered partially decalcinated compositions when ordered structure(s) were available at such compositions: else, the computational costs become intractable. Specifically, only two distinct cases of partial Ca extraction appeared in our search, namely, CaV_2O_6 and $\text{Ca}_3\text{Cu}_6\text{O}_{12}$. Also, for the two eventual candidates proposed in this work, CaNb_2O_4 and CaV_2O_4 , we did consider some Ca configurations at partial decalcination, as illustrated by the voltage curves plotted in Figure S1 in the Supporting Information (SI). Wherever possible, we have identified discharge/charge structure pairs that would enable a topotactic Ca (de)intercalation. If the charged composition exhibits multiple polymorphs, we only consider the structure that topotactically matches the discharged structure and the ground-state structure (if different from topotactically matched structure) for further calculations. After this step, the number of possible $\text{Ca}_i\text{TM}_j\text{Z}_k$ electrodes further reduced to 66.

4. Identification of the final set of 10 materials to investigate with first-principles calculations. We arrived at our final set by eliminating all of the $\text{Ca}_i\text{TM}_j\text{Z}_k$ structures which appeared thermodynamically unstable, as quantified by the 0 K energy above the convex hull (E^{hull}) that is available on MP, on their respective compositional phased diagrams. We assumed the $\text{Ca}_i\text{TM}_j\text{Z}_k$ compounds to be unstable if their $E^{\text{hull}} > 30$ meV/atom, which has been widely accepted as a rule-of-thumb in stability-based screening studies.⁵⁹ The availability of a thermodynamically stable $\text{Ca}_i\text{TM}_j\text{Z}_k$ compound ensures that there is no thermodynamic driving force for forming detrimental conversion products, instead of Ca intercalation, upon reduction of the charged TM_jZ_k structure with Ca metal (see Table 1 and Section 5 for further discussion).^{10,60} Also, we did not impose any thermodynamic stability restriction on the deintercalated TM_jZ_k compositions (see discussion in Section 2.2).

Of the 412 $\text{Ca}_i\text{M}_j\text{Z}_k$ oxides or chalcogenides, we fully investigated the thermodynamic and kinetic properties of 10 candidates and subsequently identified two structures as

promising Ca conductors/electrode materials that merit further experimental investigation; these are: CaV_2O_4 and CaNb_2O_4 . A comprehensive list of all of the materials investigated in this study is provided in Table S1 in the SI.

2.2. Ca Intercalation Characteristics in $\text{Ca}_i\text{TM}_j\text{Z}_k$ Materials

Materials. Table 1 summarizes the intercalation characteristics of the 10 $\text{Ca}_i\text{TM}_j\text{Z}_k$ candidates, including the space groups, the ICSD or MP IDs, and E^{hull} of the discharged and charged states, the average Ca topotactic intercalation voltage (eq 2), the gravimetric capacity, and the specific energy (calculated from the theoretical average voltage) for all charged-discharged pairs. Table 1 also contains the Ca coordination number and the Ca E_m in the discharged state, as well as the current cost of the raw TMs in the $\text{Ca}_i\text{TM}_j\text{Z}_k$ compounds. We included CaV_2O_5 as the 11th compound in the list as a benchmark for our computational method. Overall, the screened set of 10 compounds in Table 1 consists of only two sulfides ($\text{CaCu}_2\text{S}_2\text{-Cu}_2\text{S}_2$ and $\text{CaMo}_6\text{S}_8\text{-Mo}_6\text{S}_8$), with the rest being oxides, testament to the significantly larger collection of available oxides that naturally form with Ca in preference to other chalcogenides. All E_m reported in Table 1 are calculated to represent the discharged structure, i.e., in the dilute Ca-vacancy limit. Also, Table 1 includes both topotactic (T) and nontopotactic (N) average intercalation voltages, where relevant.

A quick glance of Table 1 reveals that all but four discharged compounds exhibit $E^{\text{hull}} = 0$ meV/atom. Three of the metastable $\text{Ca}_i\text{TM}_j\text{Z}_k$ compounds show an $E^{\text{hull}} < 30$ meV/atom (i.e., CaV_3O_7 , $\text{Ca}_5\text{Cu}_6\text{O}_{12}$, and CaMo_6S_8). Among the 10 discharged-charged pairs considered, the charged compounds can be metastable in their respective phase diagrams. For example, the deintercalated Chevrel phase is theoretically expected to decompose as $\text{Mo}_6\text{S}_8 \rightarrow 2\text{MoS}_2 + \text{Mo}$ (ca. -88.0 kJ/mol and -908 meV). However, the Chevrel cathode has shown reversible intercalation of various ions over several cycles,^{61–63} indicating that the charged Chevrel phase is kinetically stabilized in such cases. Nevertheless, reversible Ca intercalation into the Chevrel cathode has not been yet reported so far experimentally despite previous theoretical works^{64,65} comparing the intercalation behavior of Ca to other ions, suggesting possible instability associated with topotactic Ca insertion into the Chevrel. However, the thermodynamic metastability of charged compounds may not represent a significant deterrent for the reversible operation of a Ca battery or the ability to experimentally synthesize such compounds.

Unsurprisingly, from Table 1, we realize that the largest intercalation voltages are achieved by Vanadium-containing phases, which can be attributed to higher (more positive) standard reduction potential for V (e.g., $\text{V}^{\text{IV}}/\text{V}^{\text{III}}$ $+0.34$ V vs SHE) compared to the other transition metals considered (e.g., $\text{Mo}^{\text{IV}}/\text{Mo}^{\text{III}}$ -0.01 V vs SHE).⁶⁶ Indeed, Ca intercalates in V_3O_7 and $\alpha\text{-CaV}_2\text{O}_5$ with ~ 3.34 and ~ 3.13 V vs Ca/Ca^{2+} , significantly higher than MoO_3 (~ 2.77 V), Nb_2O_4 (~ 1.79 V), Cu_6O_{12} (~ 2.83 V), or Rh_2O_4 (~ 2.63 V). The lower voltage exhibited by V_2O_4 (~ 2.40 V) relative to the V_3O_7 and V_2O_5 frameworks can be attributed to the lower (more negative) reduction potential of the $\text{V}^{\text{IV}}/\text{V}^{\text{III}}$ than $\text{V}^{\text{V}}/\text{V}^{\text{IV}}$ redox couples.

The predicted Ca intercalation voltage in V_2O_5 is in excellent agreement with previous reports,^{37,67,68} providing credibility to our methodology. The large Ca intercalation voltages and the accessibility to several stable oxidation states makes the Vanadium phases the most attractive in terms of gravimetric capacities and specific energy density, as shown in Table 1. Also, our screening reveals other promising, previously unreported

phases, including (i) the CaIrO_3 (~ 3.29 V vs Ca/Ca^{2+}), (ii) $\text{Ca}_5\text{Cu}_6\text{O}_{12}$, and (iii) CaRh_2O_4 . We do not expect Ir and Rh compounds to be competitive with V compounds due to the significantly high cost of the raw metals.

During (de)intercalation, if the host framework (i.e., TM_jZ_k) does not phase transform, resulting in the symmetry of the host lattice being preserved, the (de)intercalation process is said to be topotactic. However, several cathode materials, among those that we have considered, are expected to undergo phase transformations upon Ca deintercalation, which can result in a different structure (and/or symmetry) of the charged TM_jZ_k compared to the discharged $\text{Ca}_i\text{TM}_j\text{Z}_k$ compound. Upon Ca extraction CaNb_2O_4 is thermodynamically driven to transform from the orthorhombic (space group: $Pbcm$) to tetragonal ($I4_1/a$) (see Table 1). For battery operation, topotactic intercalation mechanisms are preferred since phase transformations can lead to undesired straining (and/or fracture) of cathode particles, resulting in impedance build-up and even loss of electrochemical activity. In general, nontopotactic intercalation mechanisms are caused by the high instability of the topotactic charged phase (e.g., $\delta\text{-V}_2\text{O}_5$ for Ca) with respect to the corresponding (more stable) nontopotactic charged phase ($\alpha\text{-V}_2\text{O}_5$ for Ca). Hence, the lower the difference in stability between the topotactic and nontopotactic phases, which can be quantified by the difference between the topotactic and nontopotactic voltages, the lower the tendency for a host framework to adopt a nontopotactic intercalation mechanism.

We have highlighted the difference between the topotactic (light blue bar) and nontopotactic (green hatched bar) computed intercalation voltages for all 10 identified candidates (and $\alpha\text{-V}_2\text{O}_5$) in Figure 2. Importantly, the largest difference

experimentally reported, but the charged $Pnma$ - V_2O_4 phase is metastable (by ~ 26 meV/atom) than the stable $P4_3/mnm$ - V_2O_4 phase, leading to a topotactic (nontopotactic) voltage of ~ 2.40 V (~ 2.34 V) vs Ca/Ca^{2+} (see Figure 2). Given the small change between the topotactic and nontopotactic voltages for V_2O_4 , we speculate that the $Pnma$ - V_2O_4 polymorph may benefit from kinetic stabilization. The conversion voltage upon discharge in $\text{Ca}_3\text{Cu}_6\text{O}_{12}$ (purple bar), is higher than the nontopotactic intercalation voltage, in agreement with the metastability of the discharged $\text{Ca}_5\text{Cu}_6\text{O}_{12}$ structure (Table 1). In the case of CaV_3O_7 , the conversion voltage is only marginally higher than nontopotactic intercalation voltage, as indicated by the slight instability of V_3O_7 ($E^{\text{hull}} \sim 2$ meV/atom). However, given the larger topotactic intercalation voltage, we can expect the topotactic intercalation reaction to be kinetically favored in both the $\text{Ca}_5\text{Cu}_6\text{O}_{12}$ - $\text{Ca}_3\text{Cu}_6\text{O}_{12}$ and CaV_3O_7 - V_3O_7 systems. Nevertheless, topotactic (de)intercalation in multivalent systems are in general more complex than monovalent (Li/Na) systems,^{10,11} as highlighted by recent studies that have demonstrated decomposition reactions upon Ca extraction in CaTaN_2 ,⁴³ and phase transformations upon Ca removal in $\text{Ca}_3\text{Co}_2\text{O}_6$.⁶⁹

2.3. Ca^{2+} Migration Barriers. Excluding Mo_6S_8 that has already been studied extensively as a multivalent cathode,¹⁰ we computed the migration barriers for $\text{Ca}^{2+} E_m$ for the remaining nine materials of Table 1. All computed migration energy paths are shown in Section S4 in the SI. We have calculated the E_m for all materials assuming the dilute vacancy limit, where Ca migration occurs via a vacancy-migration mechanism, unless otherwise specified. Despite our best efforts, we were unable to converge the E_m for $\text{Ca}_5\text{Cu}_6\text{O}_{12}$ structure and thus have not reported its E_m in this work. Notably, our computed E_m of 1869 meV in $\alpha\text{-CaV}_2\text{O}_5$ (see Figure S10 in the SI) is in excellent agreement with a previous calculation (~ 1900 meV) done in the dilute vacancy limit.³⁷

Figure 3 shows the computed Ca migration barriers in selected materials (see colored shapes) vs their predicted specific energies (y-axis). Black empty circles in Figure 3 indicate previously reported E_m for different materials from Arroyo-de Dompablo and collaborators,¹¹ which serve as useful reference points for our candidates. The green region in Figure 3 marks the range of tolerable migration barriers E_m . In Figure 3, dashed lines at ~ 525 and at ~ 895 meV correspond to Ca (de)intercalation across a micron-sized cathode particle at 298 K and C/2 rate, and Ca (de)intercalation across a 10 nm cathode particle, at 333 K (~ 60 °C) and C/6 rate (6 h), respectively.^{10,32,33} The variation of the maximum tolerable E_m vs particle size, C-rate, and temperature is given in Figure S2 in the SI.

Three main observations can be made from Figure 3 and Table 1: (i) the computed barriers for all of these materials are found to be larger than the ~ 650 meV threshold of Rong et al.,³² with $\text{Ca}_2\text{V}_2\text{O}_6$ displaying the largest E_m of ~ 3235 meV; (ii) of the 10 materials investigated, only two materials CaNb_2O_4 (~ 785 meV) and CaV_2O_4 (~ 654 meV) qualify the mobility criterion since their predicted E_m are under the highest threshold of 895 meV; and (iii) the specific energy of CaV_2O_4 is quite competitive with other compounds previously reported by Arroyo-de Dompablo et al.,¹¹ and far exceeds commercial Li-ion cathodes.⁸ Although eight out of the 10 shortlisted candidates display exceedingly large Ca^{2+} migration barriers, we believe there is value in communicating these high E_m values to not only focus experimental effort on the promising candidates but also to

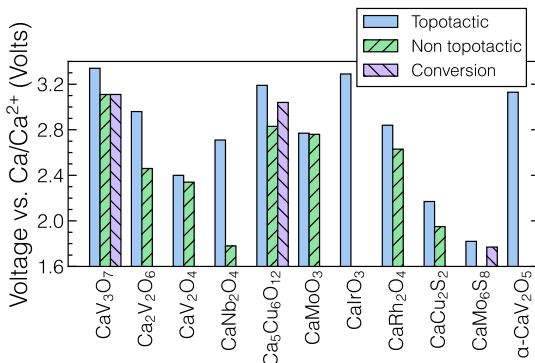


Figure 2. Computed intercalation voltages vs Ca/Ca^{2+} of compounds in Table 1. Light blue and hatched green bars indicate voltages associated with topotactic and nontopotactic mechanisms of Ca intercalation, respectively. Missing green bars indicate the unavailability of nontopotactic TM_jZ_k compounds in the ICSD or MP. The competitive conversion reactions are shown as purple hatched bars. The conversion voltage of the Chevrel phase $\text{Mo}_6\text{S}_8 + 2\text{Ca} \rightarrow 3\text{MoS}_2 + 3\text{Mo} + 3\text{CaS}$ is comparable to the topotactic insertion voltage, which is due to Mo_6S_8 being thermodynamically unstable (~ 66 meV E^{hull} , Table 1).

between topotactic and nontopotactic voltage is observed in $\text{CaNb}_2\text{O}_4 \rightarrow \text{Nb}_2\text{O}_4$ of ~ 1.0 V, with other compounds showing smaller differences between the two voltages. Note that even in frameworks presenting a significant difference between the topotactic and nontopotactic voltages (i.e., a few tenths of a V), the topotactic mechanism may remain active since, this process is typically kinetically favored over the nontopotactic intercalation. For example, the $Pnma$ phase of CaV_2O_4 is

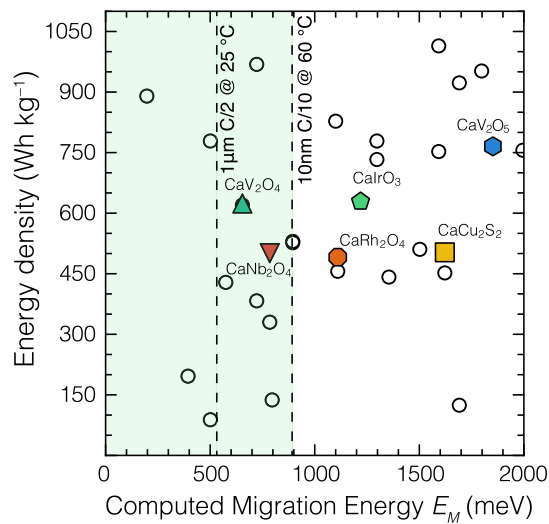


Figure 3. Computed Ca^{2+} migration barriers (in meV) plotted with respect to the predicted specific energies (in Wh/kg). Colored points are materials investigated in this study, and empty circles are computationally predicted data points from ref 11. The green ribbon shows favorable Ca^{2+} migration barriers. Reported energy densities rely on topotactic intercalation voltages, which indicate the most probable Ca insertion reactions. Specific tolerable migration barriers (i.e., 525 and 895 meV) at specific (dis)charge conditions are marked by dashed lines.^{10,32,33} Materials considered in our study that exhibit barriers above 2000 meV (CaV_3O_7 , $\text{Ca}_2\text{V}_2\text{O}_6$, and CaMoO_3) are not shown in the figure.

reformulate the design rules that can aid in designing better Ca conductors.

2.4. Assessment of CaV_2O_4 and CaNb_2O_4 Electrodes.

2.4.1. $Pnma$ - CaV_2O_4 , Post-Spinel. The structure of CaV_2O_4 arranges in the post-spinel-type prototype (also referred to as the calcium ferrite structure), where the vanadium resides in

distorted edge-sharing and corner-sharing VO_6 octahedral units (Figure 4a). The post-spinel structure has been described in detail elsewhere,⁷⁰ where Mg occupies an 8-coordinated site in the post-spinel $\text{Mg}_x\text{V}_{2-y}\text{Ti}_y\text{O}_4$. Similarly, CaV_2O_4 exhibits Ca^{2+} in an 8-coordinated environment with Ca migration occurring along one-dimensional (1D) channels in the c direction (see Figure 4a). Therefore, $Pnma$ - CaV_2O_4 is a 1D conductor, leading to a migration topology of $8 \rightarrow 5 \rightarrow 3 \rightarrow 5 \rightarrow 8$ between two equivalent Ca sites. The migration energy path of Figure 4c reaches its maximum (~654 meV) when Ca is in a 3-coordinated (triangular) site. Post-spinel structures have been previously considered for Ca intercalation. For example, Dompablo et al.⁴⁷ have studied Ca intercalation in the CaMn_2O_4 (CM)- and CaFe_2O_4 (CF)-type post-spinel structures of CaMn_2O_4 composition.

2.4.2. $Pbcm$ - CaNb_2O_4 , Layered. In CaNb_2O_4 , Nb atoms are 6-coordinated by oxygen atoms forming edge-sharing, distorted triangular NbO_6 prisms, which give rise to the layered structure in Figure 4b. Ca^{2+} ions occupy an ordered configuration of 6-coordinated irregular prismatic sites residing in-between the NbO_6 layers. Therefore, CaNb_2O_4 can be considered as a two-dimensional (2D) conductor. The in-layer migration of Ca^{2+} follows a topology $6 \rightarrow 4 \rightarrow 6$, with a maxima of ~785 meV at the 4-coordinated (rectangular) site, as indicated by Figure 4c. As highlighted by the solid and dash curved arrows in Figure 4b, we have computed the migration barrier of half of the total path, which explains the slight difference between the energies of the ground-state structures (at 0 and 100 %, Figure 4c).

3. DISCUSSION

So far, the identification of promising intercalation cathode materials has been limited by the relatively large ionic size of Ca^{2+} , which decreases the availability of structural frameworks compatible with hosting and transporting Ca^{2+} ions.⁷¹ In this report, we have searched the chemical space of ternary

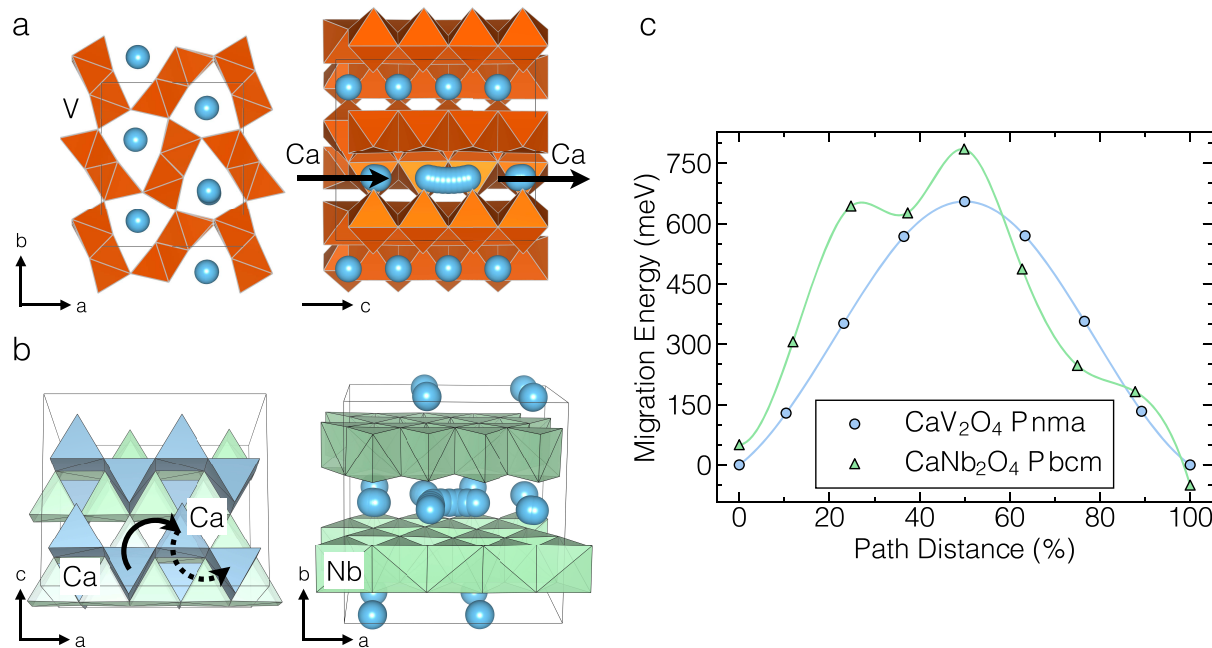


Figure 4. (a, b) Structural features of CaV_2O_4 (with space group: $Pnma$) and CaNb_2O_4 ($Pbcm$) highlighting the Ca^{2+} migration path. V and Nb-oxygen polyhedra are depicted in orange and green, respectively, while Ca is shown either as blue spheres or polyhedra. Arrows indicate the direction of Ca^{2+} migration. (c) Computed migration energy paths (in meV) of CaV_2O_4 (blue circles) and CaNb_2O_4 (green triangles) vs Ca^{2+} displacement.

$\text{Ca}_i\text{TM}_j\text{Z}_k$ compositions using a combination of existing databases, chemically intuitive filtering criteria, and DFT calculations. From an initial pool of 412 Ca-containing materials found in the ICSD, we shortlisted 10 promising candidates, whose intercalation properties were assessed further via *ab initio* methods. Our screening strategy (in Figure 1) is robust as it also provides known candidates that have been previously studied experimentally (and computationally) as Ca cathodes. While TiS_2 has been demonstrated to intercalate reversibly Ca^{2+} ,^{41,42} our screening criteria could not reveal this compound, as a stoichiometric calciated structure, i.e., Ca_xTiS_2 , is presently unknown. However, the robustness of our strategy is validated by the rediscovery of chevrel- Mo_6S_8 and CaMoO_3 phases that have received attention as Ca electrodes.^{44,48,53} Our screening procedure did not identify the following compounds which have been studied computationally before: $\text{Ca}_4\text{Fe}_9\text{O}_{17}$ has a low E_m (~ 720 meV)⁵² but does not have a matching, ordered, charged structure, and $\text{Ca}_3\text{Co}_4\text{O}_9$ exhibits E_m (~ 900 meV)⁵¹ but is significantly unstable ($E_{\text{hull}} \sim 73$ meV/atom⁵⁸). Furthermore, we did not consider $\text{Ca}_3\text{Co}_2\text{O}_6$ as a possible candidate since previous experimental studies have reported the structure to undergo an irreversible phase transformation upon Ca extraction.⁵¹

Using a different computational screening strategy, Zhang et al.⁷² did consider CaNb_2O_4 as a possible intercalation electrode for Ca batteries. Unfortunately, the authors discarded CaNb_2O_4 on the basis of the high computed E_m (~ 2100 meV). We believe that Zhang et al.⁷² computed the E_m for Ca migration through the sterically constrained O–O dumbbell that is shared between adjacent prismatic sites instead of considering the migration mechanism via a quadrilateral planar (see Section 3.2 for more detailed explanation) transition state. Ca migration through the O–O dumbbell may have been caused due to one or both of the following reasons: (i) the authors attempted to calculate the full migration path, thereby not having an additional Ca-vacancy that can aid migration (see Figure 4b), and (ii) the authors did not initialize their nudged elastic band (NEB)⁷³ calculation via the quadrilateral planar transition state.

Given the scarcity of known good Ca conductors,¹¹ our strategy emphasizes the identification of compounds providing facile Ca transport, apart from our criteria including the availability of charged structures and overall thermodynamic stability, while Zhang et al.'s strategy prioritized Ca-intercalation voltages and capacities,⁷² which tends to overlook more practical candidates.

3.1. Established Design Rules to Identify Good Ionic Conductors. It is important to take a look at the three rules to identify good multivalent conductors, initially proposed by Rong et al.,³² and examine their applicability with our findings (see Table 2 for a summary). Note that the rules were initially devised for the discovery of good Mg candidates and had not been extensively tested in Ca-containing compounds. The rules are:

1. Avoid host structures where the active ion, Ca^{2+} , resides in its preferred anion coordination environment. A previous statistical analysis of the ICSD^{54,55} showed that Ca^{2+} highly prefers a coordination number of 8 and above in oxides.⁵⁶ The preferred coordination environment of Ca^{2+} in chalcogenides, such as S, Se, and Te, has not been yet quantified rigorously. As a result, a good Ca conductor should display a Ca coordination number < 8 in oxides according to this rule. However, one of the two

good conductors that we have found in our search, CaV_2O_4 does have Ca residing in an 8 coordination environment. In contrast, CaCu_2S_2 exhibits a high E_m (~ 1622 meV) despite Ca occupying an un-preferred octahedral environment. With respect to the limited number of structures considered in this study, this rule does not seem to be a good classifier of good vs bad Ca diffusers. Hence, it is important to update this rule by examining its applicability on an even larger and more diverse dataset.

2. Reduce changes in the coordination number of the active ion (Ca^{2+}) during its migration. This rule proposes that smaller changes in coordination environment along the migration path of Ca^{2+} flatten the potential energy landscape, in turn reducing E_m .^{32,35} We could find several exceptions to this rule in the set of materials that we have considered. For example, CaV_2O_4 , CaIrO_3 , CaRh_2O_4 , CaMoO_3 , and CaV_2O_5 have similar coordination number change from stable to transition state (i.e., $8 \rightarrow 3$), yet display widely different migration barriers (654–2072 meV). CaV_3O_7 , $\text{Ca}_2\text{V}_2\text{O}_6$, and CaCu_2S_2 all have relatively low changes in coordination number, namely, $8 \rightarrow 5$, $8 \rightarrow 4$, and $6 \rightarrow 4$, than CaV_2O_4 , yet exhibit significantly higher barriers (> 1600 meV vs 654 meV). Thus, reducing coordination changes alone does not seem to be reducing the E_m in Ca compounds.
3. Increase the available volume (per number of anions) to Ca^{2+} in a given framework. In “compact” frameworks, larger volumes per anion typically correlate with weaker electrostatic interactions of Ca^{2+} with the anion (and other cations) and promote a reduction of E_m .^{32,35} Generally, larger volumes per anion can be obtained by going from oxides to sulfides (or other chalcogenides) in the same structural framework.^{35,74} This rule may not directly apply to noncompact structures, where the active ion resides in tunnel-type (e.g., hollandite MnO_2) arrangements. Here, we obtain a high barrier of 1622 meV in compact layered CaCu_2S_2 despite a sulfide anion framework. While the oxide analogue CaCu_2O_2 structure has not been reported and we cannot perform a direct comparison of migration barriers with CaCu_2S_2 , some of the post-spinel oxides (e.g., CaV_2O_4 and CaRh_2O_4) exhibit a lower barrier than CaCu_2S_2 , despite being compact frameworks (post-spinel phases are typically stable at high pressures⁷⁰).

In summary, we observe that the above rules may not be applicable to large cation⁷⁵ migration, e.g., K^+ (ca. 1.64–1.46 Å), Rb^+ (ca. 1.83–1.52 Å), Cs^+ (ca. 1.67–1.88 Å), and Ca^{2+} (ca. 1.34–1.00 Å). In particular, rule No. 1 was derived based on observations in compact anion lattices and cannot account for the diversity of geometrical and electrostatic factors appearing in more complex structural motifs, such as those sampled in our study. For example, it is known that Ca^{2+} does not occupy sites usually occupied by Li^+ or Na^+ in LiFePO_4 or NaFePO_4 ,³⁶ which is attributed both to the site preference of Ca and the underlying flexibility of the host structure to accommodate Ca. We attempt to revise the design rules for identifying good conductors, especially for frameworks with large mobile cations, in the following section.

3.2. Revised Design Rules for Identifying Good Ionic Conductors. Our motivation to formulate new design rules primarily arises from the following observations among the

Table 2. Geometric Features of the Stable and Transition States along with the E_m (in meV) Values for Materials Considered in This Work^a

material	E_m	stable state	avg. BL	transition state	D/A/V	y_{Ca}	face-sharing cation?
CaV_3O_7	2892	augmented triangular prism	2.44	rectangular pyramid	7.10 ^c	0.83	1 V at 2 Å
$Ca_2V_2O_6$	3235	biaugmented triangular prism	2.51	square planar	3.36 ^b	0.67	N/A
CaV_2O_4	654	biaugmented triangular prism	2.45	triangular	4.56	0.86	N/A
$CaNb_2O_4$	785	triangular prism	2.39	rectangular	4.42 ^b	0.51	N/A
$CaMoO_3$	2072	biaugmented triangular prism	2.55	triangular	3.82	1.03	N/A
$CaIrO_3$	1219	biaugmented triangular prism	2.46	triangular	4.32	0.91	N/A
$CaRh_2O_4$	1110	biaugmented triangular prism	2.46	triangular	4.32	0.91	N/A
$CaCu_2S_2$	1622	octahedron	2.83	tetrahedron	7.55 ^c	0.78	1 Cu at 1.57 Å
$\alpha-CaV_2O_5$	1869	distorted square antiprism	2.50	triangular	3.70	1.06	N/A

^aAvg. BL represents the average Ca-anion bond length in the stable state (in Å). D/A/V stands for diagonal/area/volume at the transition state, and in the units of Å, Å², and Å³, respectively. y_{Ca} represents the fraction of diagonal/area/volume of the transition state occupied by Ca. y_{Ca} is a dimensionless quantity. The final column indicates any presence of a face-sharing cation at the transition state. ^bShortest diagonal length reported. ^cVolumetric (three-dimensional, 3D) transition state.

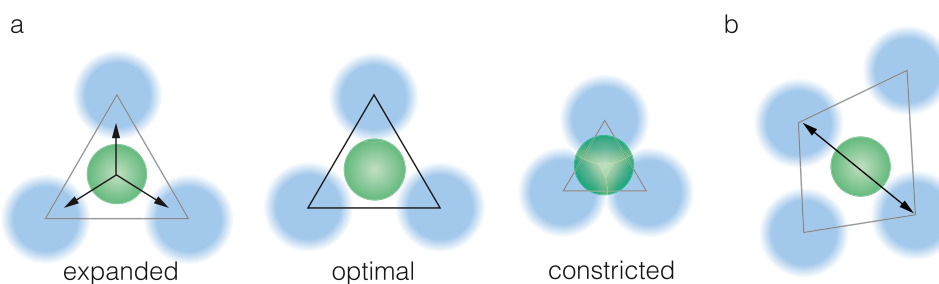


Figure 5. Ca^{2+} ions (green circles) in triangular (a) and quadrilateral (b) anion environments, which can constitute possible transition states during migration. (a) Classification of three types of triangular environments based on the triangular area, namely, expanded, optimal, and constrained. (b) The shortest diagonal of a quadrilateral transition state, along which Ca can share common tangents with anions.

calculated E_m in this work. Specifically, (i) Materials with similar structures and Ca coordination environments (at both stable and transition states) exhibit significantly different E_m . For example, CaV_2O_4 and $CaRh_2O_4$ are both post-spinel structures but show barriers that differ by nearly ~400 meV. (ii) On the other hand, materials that indeed show similar barriers exhibit remarkably different structures, such as CaV_2O_4 and $CaNb_2O_4$, $CaIrO_3$ and $CaRh_2O_4$, as well as, $CaMoO_3$ and CaV_2O_5 . (iii) The reasons for CaV_3O_7 and $Ca_2V_2O_6$ to exhibit the highest barriers among the materials considered here, are not immediately obvious.

We decided to take a deeper look into the geometrical features of the stable and transition states in the structures considered here, and our findings are summarized in Table 2. Note that our analysis is biased by the limited number and diversity of structures that we have sampled and also excludes other thermodynamic (e.g., stability or energy above the convex hull) and electronic (e.g., metallic vs nonmetallic) properties that can influence E_m . A larger dataset of migration energy profiles across a wider range of structures is thus required to fully understand and decouple the different contributions to E_m , which is beyond the scope of this work.

The biaugmented triangular prism and distorted square antiprism in Table 2 correspond to 8-coordinated (stable) sites of Ca and the augmented triangular prism refers to a 7-coordinated site. Avg. BL (in Å) refers to the average Ca-anion bond length in the stable site of each structure. While triangular, rectangular, and square planars are 2D (planar) transition states, rectangular pyramid and tetrahedron are 3D (volumetric). D/A/V in Table 2 represents the length of the diagonal (in Å) for a quadrilateral transition state, the area (in Å²) of a triangular

transition state, and the volume (in Å³) of a volumetric transition state (i.e., a three-dimensional or a 3D space), respectively. y_{Ca} represents the fraction of the diagonal/area/volume occupied by Ca at the transition state, and the final column of Table 2 indicates the presence (or not) of a face-sharing cation and its distance from the migrating Ca, at a volumetric transition state. For identifying the number of Ca-anion bonds at the transition state (and hence to calculate the geometrical features of the transition state), we used the longest Ca-anion bond length at the stable state as the upper limit for each structure considered.

Note that all geometrical features reported in Table 2 are obtained from a DFT-relaxed geometry of the ground states (endpoint structures). The endpoint configurations are typically relaxed before doing the NEB calculation and they are not altered during the course of a NEB procedure. The features reported are for a nonmigrating Ca ion, i.e., we take the DFT-relaxed endpoint structure and label a Ca ion that is nonmigrating but is symmetrically equivalent to the migrating Ca. Subsequently, we construct a (hypothetical) migration path for the labeled Ca ion, which mimics the set of images that are used as a starting point for the NEB, locate the transition state along the as-constructed migration path and estimate the geometrical features of the located transition state. Here, we focus on a nonrelaxed migration path of a nonmigrating Ca ion to ensure that we include any “global” structure relaxations (e.g., any changes in lattice parameters) of the endpoint structures while excluding any “local” structure relaxations that result from the relaxation of the endpoint configuration at the site of the migrating Ca.

We can infer from Table 2 that the most common stable and transition states are 8-coordinated and 3-coordinates sites, respectively, exhibiting a wide range in E_m from 654 to 2072 meV. Since the stable 8-coordinated sites do not differ significantly in terms of average BL (2.45–2.51 Å), we expect the variations in observed E_m , in such frameworks, to primarily arise from the differences in the transition state. For example, if Ca is migrating through a triangular transition state, as shown in Figure 5a, an “optimal” size of the triangular transition state will ensure a lower E_m compared to scenarios where the triangle is too expanded or too constricted.

If we assume a rigid sphere model of atoms in a framework, the optimal triangular framework is where the central Ca atom (green spheres in Figure 5a) shares common tangents with the three oxygen atoms (blue spheres) that form the vertices of the triangle. Given an ionic radius⁷⁵ of Ca^{2+} and O^{2-} to be ~1.12 and ~1.38 Å, respectively, we can calculate the fraction of the triangular area occupied by Ca (y_{Ca}) under the optimal condition to be ~0.48. In the case of a triangular transition state with S^{2-} vertices (ionic radius of S^{2-} ~1.84 Å),⁷⁵ optimal y_{Ca} will be 0.35. Hence, triangular transition states that have y_{Ca} closer to the optimal value will have a lower E_m . Similar optimal conditions can be derived for other types of transition states as well. In the case of a quadrilateral-type transition state (Figure 5b), such as square planar or rectangular, the rigid sphere of Ca^{2+} has to share common tangents with the anion vertices along the shortest diagonal. Thus, for O^{2-} and S^{2-} quadrilateral vertices, the optimal fraction of the diagonal that should be occupied by Ca^{2+} is 0.45 and 0.38, respectively. Analogously, the optimal volume fraction that Ca^{2+} should occupy in a tetrahedron with O^{2-} (S^{2-}) vertices is 0.73 (0.44), while in the case of a square pyramid, the optimal volume fraction with O^{2-} vertices is 0.28—in a square pyramid, only half of the Ca sphere will be fully contained within the pyramid. The optimal y_{Ca} in sulfide frameworks will be lower than oxide analogues due to the larger ionic radius of S^{2-} compared to O^{2-} .

We can explain important trends observed in Table 2 based on the deviation of the transition state away from the optimal condition mentioned above. For example, the y_{Ca} of the triangular transition state in CaV_2O_4 is closer to the optimal triangle by ~0.05 than the y_{Ca} of CaRh_2O_4 , which causes a lowering of E_m by ~400 meV in CaV_2O_4 . Both CaV_2O_4 and CaRh_2O_4 are post-spinels with nearly identical stable sites, which indicates the importance of the small deviations in the transition state on the overall barrier. Interestingly, y_{Ca} in CM- and CF-type post-spinels of composition CaMn_2O_4 are 0.97 and 0.91, respectively, as calculated from the corresponding DFT-relaxed bulk structures available in the MP. These y_{Ca} values are in excellent agreement with previously reported⁴⁷ E_m values, i.e., ~1850 meV in CM and ~1350 meV in CF CaMn_2O_4 , further validating our optimal y_{Ca} criterion. CaNb_2O_4 exhibits a quadrilateral transition state (rectangular, Figure 4b) whose y_{Ca} is closer to the optimal value by ~0.16 than the y_{Ca} of $\text{Ca}_2\text{V}_2\text{O}_6$, causing a lowering of ~2400 meV of E_m in CaNb_2O_4 . Furthermore, CaRh_2O_4 and CaIrO_3 both exhibit similar barriers (difference of ~100 meV) owing to similar y_{Ca} in the transition state, while the E_m values of CaMoO_3 and CaV_2O_5 differ marginally (~200 meV) due to changes in y_{Ca} (~0.03) at their triangular transition states. Although we do not expect the relationship between the deviation from optimality and E_m to be linear, we can expect a transition state that is closer to its optimality to yield a lower E_m .

The presence (or lack of) nonmigrating cations, such as transition metals, or other cations, e.g., S^{6+} , P^{5+} , etc., that share a “face” with a volumetric transition state, can also have a non-negligible impact on the values of E_m . Indeed, the high barriers in CaV_3O_7 and CaCu_2S_2 can be attributed, to a large extent, to the face-sharing V and Cu atoms, respectively, at the transition state during Ca migration. Such face-sharing cations can cause a significant increase in electrostatic potential energy due to electrostatic repulsion, particularly at small separations from the migrating Ca, resulting in a higher barrier. For example, the Ca–Cu distance in CaCu_2S_2 at the transition state (~1.57 Å) is significantly lower than the Ca–S bond distance in the same site (~2.45 Å), signifying that the Ca–Cu electrostatic repulsion is insufficiently screened by the surrounding anion framework, resulting in the high E_m (~1622 meV) observed. In general, we expect face-sharing cations to have a higher impact on E_m in oxides than sulfides (or other chalcogenides), in line with previous observations,⁷⁶ due to the higher ionicity of oxygen-containing bonds and the lack of electrostatic screening by O^{2-} compared to S^{2-} ,¹⁰ partly explaining the higher E_m in CaV_3O_7 than CaCu_2S_2 . Also, there are examples of electrostatic repulsion forcing multivalent ions to migrate through a sterically constrained anion–cation–anion dumbbell site instead of a planar or a volumetric transition site,⁷⁶ always resulting in higher barriers.

Apart from optimal transition states and face-sharing cations, we speculate that structures that exhibit a lower Ca volume fraction change (Δv_{Ca}) during migration, to yield a lower E_m . Although we do not have a rigorous set of calculated barriers to justify this suggestion, we highlight the similarities (and differences) with rule No. 2 in Section 3.1. For a given polyhedral coordination that Ca is occupying, v_{Ca} is the fraction of the polyhedral volume occupied by a rigid Ca^{2+} sphere. Therefore, if a migration pathway minimizes Δv_{Ca} during Ca motion (i.e., reduce the change in v_{Ca} between the stable and transition states), it should, in principle, flatten the potential energy landscape, since Ca is moving across polyhedra that are “similar”. This is analogous to what is expected by minimizing changes in coordination number during migration, but results in a better metric (both quantitatively and qualitatively) to identify the similarity of polyhedral motifs during ionic migration. However, there is an inherent trade-off associated with maintaining the same v_{Ca} and attaining the optimal y_{Ca} at the transition state, which will eventually decide the magnitude of E_m . This trade-off can be approximately considered to be breaking/forming the optimal number of bonds during migration.

Finally, we suggest that volumetric/planar transition states that have more degrees of freedom (DoF, i.e., number of allowed changes of edge lengths and shapes) to attain better $v_{\text{Ca}} - y_{\text{Ca}}$ trade-offs, and result in lower E_m . Thus, we are hopeful that materials that exhibit a quadrilateral-type transition state, which has more DoF than triangular, and have E_m lower than CaNb_2O_4 (shown in this work) will be identified in the near future.

To summarize, we propose the following updated set of design rules for identifying good ionic conductors, especially for structures with large migrating cations:

1. Find structures that yield close to the optimal diagonal/area/volume (D/A/V) fraction of migrating cation at the transition state (excluding any local relaxation during migration).

2. In the case of volumetric transition states in frameworks, avoid face-sharing cations.
3. Minimize changes in the volume fraction of cation as it migrates across sites (by choosing structures exhibiting transition states with higher degrees of freedom).

4. CONCLUSIONS

In summary, we investigated the large compositional space of more than 400 ternary chalcogenides with prototypical formula $\text{Ca}_i\text{M}_j\text{Z}_k$. From this large pool of materials, 10 materials were examined using first-principles calculations. We found two previously unreported promising electrode candidates, namely, post-spinel CaV_2O_4 and layered CaNb_2O_4 , with Ca migration barriers of ~ 654 and ~ 785 meV, respectively. From the analysis of the Ca migration characteristics in the 10 selected compounds, we proposed updated design rules for the identification of good Ca conductors. These rules are to find structures: (i) with optimal diagonal/area/volume at the transition state, (ii) without any face-sharing cations at the transition state, and (iii) that minimize changes in polyhedral volumes during ion migration. While our study centered on Ca-based materials for positive electrodes, our findings may be extended to other compounds hosting large mobile cations.

5. METHODOLOGY

5.1. Ab Initio Thermodynamics of Conversion and Intercalation Voltages. An intercalation battery based on the hypothetical $\text{Ca}_n\text{TM}_j\text{Z}_k$ cathode electrode implies the reversible extraction/insertion of Ca^{2+} ions from/into the $\text{Ca}_n\text{TM}_j\text{Z}_k$ framework following the spontaneous reaction of eq 1

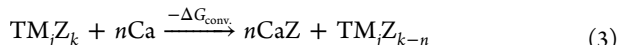


where n sets the Ca concentration and $-\Delta G_{\text{inter}}$ is the change of Gibbs energy at 0 K, where the DFT total energies are approximated as the Gibbs energies (i.e., $E \approx G$). By doing so, we neglect the pV and entropic contributions to the Gibbs energy. From eq 1, we estimate the average intercalation voltage, V_{inter} , as expressed in eq 2

$$V_{\text{inter.}} = -\frac{\Delta G_{\text{inter.}}}{2nF} = -\frac{E_{\text{Ca}_n\text{TM}_j\text{Z}_k} - [E_{\text{TM}_j\text{Z}_k} + n\mu_{\text{Ca}}]}{2nF} \quad (2)$$

where μ_{Ca} is the Ca chemical potential (set to that of Ca metal) and F is the Faraday constant. The value 2 in the denominator of eq 2 takes into account the two electrons released upon oxidation of Ca to Ca^{2+} . Note that the reaction represented by eq 1 can be either topotactic or nontopotactic in nature. Computed intercalation voltages are reported in Table 1 and Figure 2.

An alternative process to Ca intercalation is the conversion of a hypothetical TM_jZ_k cathode upon reduction with Ca, leading typically to the irreversible formation of stable binary/ternary oxides (e.g., CaO and TMO) that can detrimentally stop any electrochemical activity. Previous studies have examined the competition between intercalation and conversion reactions in a large dataset of multivalent TM oxide, sulfide, and selenide chemistries.^{10,60} As an example, a possible conversion reaction is shown in eq 3 for a hypothetical TM_jZ_k forming CaZ and $\text{TM}_j\text{Z}_{k-n}$.



A conversion voltage can be linked to such reactions, as represented by eq 4

$$\begin{aligned} V_{\text{conv.}} &= -\frac{\Delta G_{\text{conv.}}}{2nF} \\ &= -\frac{nE_{\text{CaZ}} + E_{\text{TM}_j\text{Z}_{k-n}} - [E_{\text{TM}_j\text{Z}_k} + n\mu_{\text{Ca}}]}{2nF} \end{aligned} \quad (4)$$

For intercalation reactions to be thermodynamically favorable, $V_{\text{inter.}}$ needs to be higher than $V_{\text{conv.}}$. Another way to assess whether the intercalation of Ca is favored over undesired conversion reactions is to examine the thermodynamic stability of the discharged $\text{Ca}_i\text{TM}_j\text{Z}_k$ compound with respect to a combination of all possible compounds that can exist at the same composition, which is captured by the E^{hull} . A potential cathode that exhibits $E^{\text{hull}} = 0$ meV/atom will strongly favor intercalation reactions over conversion upon reduction with Ca.

5.2. First-Principles Calculations. To assess the suitability of the $\text{Ca}_i\text{TM}_j\text{Z}_k$ compounds for Ca electrodes, we computed the migration energy E_m using the NEB method^{73,77} together with DFT calculations.^{45,46} In DFT, the total energy was approximated by the generalized gradient approximation (GGA) exchange-correlation functional as parameterized by Perdew, Burke, and Ernzerhof (or PBE),⁷⁸ which was evaluated using the code VASP.^{79,80} The electronic wavefunctions were expanded as plane waves up to a kinetic energy cutoff of 520 eV and combined with the projector-augmented wave (PAW) potentials for the core electrons.⁸¹ The PAW potentials used were, Ca_sv (06Sep2000 3s3p4s), Cu (05Jan2001 d¹⁰p¹), Ir (06Sep2000 s¹d⁸), Mo_pv (08Apr2002 4p5s4d), Nb_pv (08Apr2002 4p5s4d), O (08Apr2002 2s2p), Rh (06Sep2000 s¹d⁸), S (17Jan2003 s²p⁴), and V_pv (07Sep2000 p⁶d⁴s¹). The total energies in DFT were integrated using a k -point density of at least 1000/atom, and converged within 10^{-6} eV/cell, without imposing symmetry restrictions. The atomic forces and stresses were converged to within 10^{-2} eV/Å and 0.29 GPa, respectively.

For the estimations of the Ca intercalation voltages in $\text{Ca}_i\text{TM}_j\text{Z}_k$ compounds, which often behave as highly correlated systems,^{82–87} we employed the rotationally invariant Hubbard U approach to GGA, as proposed by Dudarev et al.,⁸⁸ resulting in a GGA + U (or PBE + U) Hamiltonian. GGA + U corrects for the spurious self-interaction error introduced by the highly localized d orbitals of the redox species V, Cu, Nb, and Mo. Note that the empirical GGA+ U correction has been extensively calibrated to compute intercalation voltages in battery materials.^{82,86,87} The specific U values used were 3.10 eV for V, 4.00 eV for Cu, 1.50 eV for Nb, and 4.38 eV for Mo, as previously reported by Jain et al.⁸⁶

Following the prescription by Chen et al.,³³ we implemented model supercells that always introduced a minimum distance ≥ 8 Å between the Ca ions participating in the ion migration, to minimize the fictitious interactions between periodic images, in our NEB^{73,77,89} calculations. We fully relaxed (i.e., coordinate, volume and shape) the initial and final states defining the Ca^{2+} migration paths in our NEB until the forces on the atoms were lower than 10^{-2} eV/Å. Note that we used the GGA functional in our initial/final state and the overall NEB calculation as well, since the GGA has been shown to be more appropriate than GGA+ U to predict ion-migration paths.³² The elastic bands in all materials considered are constructed using seven distinct, equally spaced images, between the ground-state structures (i.e., the endpoints). The forces on the elastic band are converged to within 0.05 eV/Å. All E_m estimations were done in the regime of dilute vacancy, i.e., one vacancy is created in the Ca lattice. Notably, the introduction of Ca vacancies in the potential

electrodes (as required for NEB calculations) was compensated by the spontaneous oxidation of nearby transition metal(s).

■ ASSOCIATED CONTENT

SI Supporting Information

The Supporting Information is available free of charge at <https://pubs.acs.org/doi/10.1021/acs.chemmater.1c01992>.

Structural and thermodynamic stabilities of 412 ternary chalcogenides; a model showing the maximum tolerable migration barrier vs particle size, rate, and temperature; and the computed migration energy profiles of ternary chalcogenides considered ([PDF](#))

■ AUTHOR INFORMATION

Corresponding Authors

Gopalakrishnan Sai Gautam – Department of Materials Engineering, Indian Institute of Science, Bangalore 560012, India;  orcid.org/0000-0002-1303-0976; Email: saigautamg@iisc.ac.in

Pieremanuele Canepa – Department of Materials Science and Engineering, National University of Singapore, 117575, Singapore; Department of Chemical and Biomolecular Engineering, National University of Singapore, 117585, Singapore;  orcid.org/0000-0002-5168-9253; Email: pcanepa@nus.edu.sg

Authors

Wang Lu – Department of Materials Science and Engineering, National University of Singapore, 117575, Singapore

Juefan Wang – Department of Materials Science and Engineering, National University of Singapore, 117575, Singapore

Complete contact information is available at:

<https://pubs.acs.org/10.1021/acs.chemmater.1c01992>

Notes

The authors declare no competing financial interest.

■ ACKNOWLEDGMENTS

P.C. acknowledges funding from the National Research Foundation under his NRF Fellowship NRFF12-2020-0012 and support from the Singapore Ministry of Education Academic Fund Tier 1 (R-284-000-186-133). G.S.G. acknowledges financial support from the Indian Space Research Organization-Space Technology Cell at the Indian Institute of Science, under project code number ISTC/MET/SGG/451. The computational work was performed on resources of the National Supercomputing Centre, Singapore (<https://www.nscc.sg>).

■ REFERENCES

- (1) Tarascon, J.-M. Is lithium the new gold? *Nat. Chem.* **2010**, *2*, No. 510.
- (2) Richard, V. N. The rechargeable revolution: A better battery. *Nature* **2014**, *507*, 26–28.
- (3) Larcher, D.; Tarascon, J.-M. Towards greener and more sustainable batteries for electrical energy storage. *Nat. Chem.* **2015**, *7*, 19–29.
- (4) Nykvist, B.; Nilsson, M. Rapidly falling costs of battery packs for electric vehicles. *Nat. Clim. Change* **2015**, *5*, 329–332.
- (5) Cano, Z. P.; Banham, D.; Ye, S.; Hintennach, A.; Lu, J.; Fowler, M.; Chen, Z. Batteries and fuel cells for emerging electric vehicle markets. *Nat. Energy* **2018**, *3*, 279–289.

(6) Crabtree, G. The coming electric vehicle transformation. *Science* **2019**, *366*, 422–424.

(7) Tian, Y.; Zeng, G.; Rutt, A.; Shi, T.; Kim, H.; Wang, J.; Koettgen, J.; Sun, Y.; Ouyang, B.; Chen, T.; Lun, Z.; Rong, Z.; Persson, K.; Ceder, G. Promises and Challenges of Next-Generation “Beyond Li-ion” Batteries for Electric Vehicles and Grid Decarbonization. *Chem. Rev.* **2021**, *121*, 1623–1669.

(8) Whittingham, M. S. Ultimate Limits to Intercalation Reactions for Lithium Batteries. *Chem. Rev.* **2014**, *114*, 11414–11443.

(9) Muldoon, J.; Bucur, C. B.; Gregory, T. Quest for Nonaqueous Multivalent Secondary Batteries: Magnesium and Beyond. *Chem. Rev.* **2014**, *114*, 11683–11720.

(10) Canepa, P.; Gautam, G. S.; Hannah, D. C.; Malik, R.; Liu, M.; Gallagher, K. G.; Persson, K. A.; Ceder, G. Odyssey of Multivalent Cathode Materials: Open Questions and Future Challenges. *Chem. Rev.* **2017**, *117*, 4287–4341.

(11) Arroyo-de Dompablo, M. E.; Ponrouch, A.; Johansson, P.; Palacín, M. R. Achievements, Challenges, and Prospects of Calcium Batteries. *Chem. Rev.* **2019**, *120*, 6331–6357.

(12) El Kharbachi, A. E.; Zavorotynska, O.; Latroche, M.; Cuevas, F.; Yartys, V.; Fichtner, M. Exploits, advances and challenges benefiting beyond Li-ion battery technologies. *J. Alloys Compd.* **2020**, *817*, No. 153261.

(13) Blanc, L. E.; Kundu, D.; Nazar, L. F. Scientific Challenges for the Implementation of Zn-Ion Batteries. *Joule* **2020**, *4*, 771–799.

(14) Peled, E.; Meitav, A.; Brand, M. Calcium Thionyl Chloride High-Rate Reserve Cell. *J. Electrochim Soc.* **1981**, *128*, 1936–1938.

(15) Aurbach, D.; Skaletsky, R.; Gofer, Y. The Electrochemical Behavior of Calcium Electrodes in a Few Organic Electrolytes. *J. Electrochim. Soc.* **1991**, *138*, 3536–3545.

(16) See, K. A.; Gerbec, J. A.; Jun, Y.-S.; Wudl, F.; Stucky, G. D.; Seshadri, R. A High Capacity Calcium Primary Cell Based on the Ca-S System. *Adv. Energy Mater.* **2013**, *3*, 1056–1061.

(17) Ponrouch, A.; Frontera, C.; Bardé, F.; Palacín, M. R. Towards a calcium-based rechargeable battery. *Nat. Mater.* **2016**, *15*, 169–172.

(18) Wang, D.; Gao, X.; Chen, Y.; Jin, L.; Kuss, C.; Bruce, P. G. Plating and stripping calcium in an organic electrolyte. *Nat. Mater.* **2018**, *17*, 16–20.

(19) Hahn, N. T.; Seguin, T. J.; Lau, K.-C.; Liao, C.; Ingram, B. J.; Persson, K. A.; Zavadil, K. R. Enhanced Stability of the Carba-closododecaborate Anion for High-Voltage Battery Electrolytes through Rational Design. *J. Am. Chem. Soc.* **2018**, *140*, 11076–11084.

(20) Li, Z.; Fuhr, O.; Fichtner, M.; Zhao-Karger, Z. Towards stable and efficient electrolytes for room-temperature rechargeable calcium batteries. *Energy Environ. Sci.* **2019**, *12*, 3496–3501.

(21) Shyamsunder, A.; Blanc, L. E.; Assoud, A.; Nazar, L. F. Reversible Calcium Plating and Stripping at Room Temperature Using a Borate Salt. *ACS Energy Lett.* **2019**, *4*, 2271–2276.

(22) Scafuri, A.; Berthelot, R.; Pirnat, K.; Vizintin, A.; Bitenc, J.; Aquilanti, G.; Foix, D.; Dedryvère, R.; Arçon, I.; Dominko, R.; Stievano, L. Spectroscopic Insights into the Electrochemical Mechanism of Rechargeable Calcium/Sulfur Batteries. *Chem. Mater.* **2020**, *32*, 8266–8275.

(23) Bitenc, J.; Scafuri, A.; Pirnat, K.; Lozinšek, M.; Jerman, I.; Grdadolnik, J.; Fraisse, B.; Berthelot, R.; Stievano, L.; Dominko, R. Electrochemical Performance and Mechanism of Calcium Metal-Organic Battery. *Batteries Supercaps* **2021**, *4*, 214–220.

(24) Yang, F.; Liu, Y.-S.; Feng, X.; Qian, K.; Kao, L. C.; Ha, Y.; Hahn, N. T.; Seguin, T. J.; Tsige, M.; Yang, W.; Zavadil, K. R.; Persson, K. A.; Guo, J. Probing calcium solvation by XAS, MD and DFT calculations. *RSC Adv.* **2020**, *10*, 27315–27321.

(25) Gao, X.; Liu, X.; Mariani, A.; Elia, G. A.; Lechner, M.; Streb, C.; Passerini, S. Alkoxy-functionalized ionic liquid electrolytes: understanding ionic coordination of calcium ion speciation for the rational design of calcium electrolytes. *Energy Environ. Sci.* **2020**, *13*, 2559–2569.

(26) Liang, Y.; Dong, H.; Aurbach, D.; Yao, Y. Current status and future directions of multivalent metal-ion batteries. *Nat. Energy* **2020**, *5*, 646–656.

- (27) Forero-Saboya, J.; Davoisne, C.; Dedryvère, R.; Yousef, I.; Canepa, P.; Ponrouch, A. Understanding the nature of the passivation layer enabling reversible calcium plating. *Energy Environ. Sci.* **2020**, *13*, 3423–3431.
- (28) Hahn, N. T.; Driscoll, D. M.; Yu, Z.; Sterbinsky, G. E.; Cheng, L.; Balasubramanian, M.; Zavadil, K. R. Influence of Ether Solvent and Anion Coordination on Electrochemical Behavior in Calcium Battery Electrolytes. *ACS Appl. Energy Mater.* **2020**, *3*, 8437–8447.
- (29) Hahn, N. T.; Self, J.; Seguin, T. J.; Driscoll, D. M.; Rodriguez, M. A.; Balasubramanian, M.; Persson, K. A.; Zavadil, K. R. The critical role of configurational flexibility in facilitating reversible reactive metal deposition from borohydride solutions. *J. Mater. Chem. A* **2020**, *8*, 7235–7244.
- (30) Li, Z.; Vinayan, B. P.; Diemant, T.; Behm, R. J.; Fichtner, M.; Zhao-Karger, Z. Rechargeable Calcium-Sulfur Batteries Enabled by an Efficient Borate-Based Electrolyte. *Small* **2020**, *16*, No. 2001806.
- (31) Xu, Z.-L.; Park, J.; Wang, J.; Moon, H.; Yoon, G.; Lim, J.; Ko, Y.-J.; Cho, S.-P.; Lee, S.-Y.; Kang, K. A new high-voltage calcium intercalation host for ultra-stable and high-power calcium rechargeable batteries. *Nat. Commun.* **2021**, *12*, No. 3369.
- (32) Rong, Z.; Malik, R.; Canepa, P.; Gautam, G. S.; Liu, M.; Jain, A.; Persson, K.; Ceder, G. Materials Design Rules for Multivalent Ion Mobility in Intercalation Structures. *Chem. Mater.* **2015**, *27*, 6016–6021.
- (33) Chen, T.; Gautam, G. S.; Canepa, P. Ionic Transport in Potential Coating Materials for Mg Batteries. *Chem. Mater.* **2019**, *31*, 8087–8099.
- (34) Bölle, F. T.; Mathiesen, N. R.; Nielsen, A. J.; Vegge, T.; Garcia-Lastra, J. M.; Castelli, I. E. Autonomous Discovery of Materials for Intercalation Electrodes. *Batteries Supercaps* **2020**, *3*, 488–498.
- (35) Canepa, P.; Bo, S.-H.; Gautam, G. S.; Key, B.; Richards, W. D.; Shi, T.; Tian, Y.; Wang, Y.; Li, J.; Ceder, G. High magnesium mobility in ternary spinel chalcogenides. *Nat. Commun.* **2017**, *8*, No. 1759.
- (36) Kim, S.; Yin, L.; Lee, M. H.; Parajuli, P.; Blanc, L.; Fister, T. T.; Park, H.; Kwon, B. J.; Ingram, B. J.; Zapol, P.; Klie, R. F.; Kang, K.; Nazar, L. F.; Lapidus, S. H.; Vaughey, J. T. High-Voltage Phosphate Cathodes for Rechargeable Ca-Ion Batteries. *ACS Energy Lett.* **2020**, *5*, 3203–3211.
- (37) Gautam, G. S.; Canepa, P.; Malik, R.; Liu, M.; Persson, K.; Ceder, G. First-principles evaluation of multi-valent cation insertion into orthorhombic V_2O_5 . *Chem. Commun.* **2015**, *51*, 13619–13622.
- (38) Amatucci, G. G.; Badway, F.; Singhal, A.; Beaudoin, B.; Skandan, G.; Bowmer, T.; Plitz, I.; Pereira, N.; Chapman, T.; Jaworski, R. Investigation of Yttrium and Polyvalent Ion Intercalation into Nanocrystalline Vanadium Oxide. *J. Electrochem. Soc.* **2001**, *148*, No. A930.
- (39) Verrelli, R.; Black, A.; Pattanathummasid, C.; Tchitchevka, D.; Ponrouch, A.; Oró-Solé, J.; Frontera, C.; Bardé, F.; Rozier, P.; Palacín, M. On the strange case of divalent ions intercalation in V_2O_5 . *J. Power Sources* **2018**, *407*, 162–172.
- (40) Murata, Y.; Takada, S.; Obata, T.; Tojo, T.; Inada, R.; Sakurai, Y. Effect of water in electrolyte on the Ca^{2+} insertion/extraction properties of V_2O_5 . *Electrochim. Acta* **2019**, *294*, 210–216.
- (41) Tchitchevka, D. S.; Ponrouch, A.; Verrelli, R.; Broux, T.; Frontera, C.; Sorrentino, A.; Bardé, F.; Biskup, N.; de Dompablo, M. E. A.; Palacín, M. R. Electrochemical Intercalation of Calcium and Magnesium in TiS_2 : Fundamental Studies Related to Multivalent Battery Applications. *Chem. Mater.* **2018**, *30*, 847–856.
- (42) Verrelli, R.; Black, A.; Dugas, R.; Tchitchevka, D.; Ponrouch, A.; Palacín, M. R. Steps Towards the Use of TiS_2 Electrodes in Ca Batteries. *J. Electrochim. Soc.* **2020**, *167*, No. 070532.
- (43) Verrelli, R.; Black, A. P.; Frontera, C.; Oró-Solé, J.; de Dompablo, M. E. A.; Fuertes, A.; Palacín, M. R. On the Study of Ca and Mg Deintercalation from Ternary Tantalum Nitrides. *ACS Omega* **2019**, *4*, 8943–8952.
- (44) Cabello, M.; Nacimiento, F.; Alcántara, R.; Lavela, P.; Vicente, C. P.; Tirado, J. L. Applicability of Molybdate as an Electrode Material in Calcium Batteries: A Structural Study of Layer-type Ca_xMoO_3 . *Chem. Mater.* **2018**, *30*, 5853–5861.
- (45) Hohenberg, P.; Kohn, W. Inhomogeneous Electron Gas. *Phys. Rev.* **1964**, *136*, B864–B871.
- (46) Kohn, W.; Sham, L. J. Self-Consistent Equations Including Exchange and Correlation Effects. *Phys. Rev.* **1965**, *140*, A1133–A1138.
- (47) Dompablo, M. E. A. D.; Krich, C.; Nava-Avendaño, J.; Biskup, N.; Palacín, M. R.; Bardé, F. A Joint Computational and Experimental Evaluation of $CaMn_2O_4$ Polymorphs as Cathode Materials for Ca Ion Batteries. *Chem. Mater.* **2016**, *28*, 6886–6893.
- (48) Arroyo-de Dompablo, M. E.; Krich, C.; Nava-Avendaño, J.; Palacín, M. R.; Bardé, F. In quest of cathode materials for Ca ion batteries: the $CaMO_3$ perovskites ($M = Mo, Cr, Mn, Fe, Co$, and Ni). *Phys. Chem. Chem. Phys.* **2016**, *18*, 19966–19972.
- (49) Torres, A.; Luque, F.; Tortajada, J.; de Dompablo, M. A. DFT investigation of Ca mobility in reduced-perovskite and oxidized-makorite oxides. *Energy Storage Mater.* **2019**, *21*, 354–360.
- (50) Torres, A.; Casals, J. L.; de Dompablo, M. E. A. Enlisting Potential Cathode Materials for Rechargeable Ca Batteries. *Chem. Mater.* **2021**, *33*, 2488–2497.
- (51) Torres, A.; Bardé, F.; de Dompablo, M. A. Evaluation of cobalt oxides for calcium battery cathode applications. *Solid State Ionics* **2019**, *340*, No. 115004.
- (52) Black, A. P.; Torres, A.; Frontera, C.; Palacín, M. R.; de Dompablo, M. E. A. Appraisal of calcium ferrites as cathodes for calcium rechargeable batteries: DFT, synthesis, characterization and electrochemistry of $Ca_4Fe_9O_{17}$. *Dalton Trans.* **2020**, *49*, 2671–2679.
- (53) Rogosic, J. Towards the Development of Calcium Ion Batteries. Ph.D. Thesis, Massachusetts Institute of Technology, Department of Materials Science and Engineering, 2014.
- (54) Bergerhoff, G.; Hundt, R.; Sievers, R.; Brown, I. D. The inorganic crystal structure data base. *J. Chem. Inf. Comput. Sci.* **1983**, *23*, 66–69.
- (55) Hellenbrandt, M. The Inorganic Crystal Structure Database (ICSD)-Present and Future. *Crystallogr. Rev.* **2004**, *10*, 17–22.
- (56) Brown, I. D. What factors determine cation coordination numbers? *Acta Crystallogr., Sect. B: Struct. Sci.* **1988**, *44*, 545–553.
- (57) Yang, L.; Dacek, S.; Ceder, G. Proposed definition of crystal substructure and substructural similarity. *Phys. Rev. B* **2014**, *90*, No. 054102.
- (58) Jain, A.; Ong, S. P.; Hautier, G.; Chen, W.; Richards, W. D.; Dacek, S.; Cholia, S.; Gunter, D.; Skinner, D.; Ceder, G.; Persson, K. A. Commentary: The Materials Project: A materials genome approach to accelerating materials innovation. *APL Mater.* **2013**, *1*, No. 011002.
- (59) Sun, W.; Dacek, S. T.; Ong, S. P.; Hautier, G.; Jain, A.; Richards, W. D.; Gamst, A. C.; Persson, K. A.; Ceder, G. The thermodynamic scale of inorganic crystalline metastability. *Sci. Adv.* **2016**, *2*, No. e1600225.
- (60) Hannah, D. C.; Gautam, G. S.; Canepa, P.; Ceder, G. On the Balance of Intercalation and Conversion Reactions in Battery Cathodes. *Adv. Energy Mater.* **2018**, *8*, No. 1800379.
- (61) Levi, E.; Gofer, Y.; Vestfreed, Y.; Lancry, E.; Aurbach, D. $Cu_2Mo_6S_8$ Chevrel Phase, A Promising Cathode Material for New Rechargeable Mg Batteries: A Mechanically Induced Chemical Reaction. *Chem. Mater.* **2002**, *14*, 2767–2773.
- (62) Levi, M. D.; Lancry, E.; Levi, E.; Gizbar, H.; Gofer, Y.; Aurbach, D. The effect of the anionic framework of MoX Chevrel Phase ($X=S$, Se) on the thermodynamics and the kinetics of the electrochemical insertion of Mg ions. *Solid State Ionics* **2005**, *176*, 1695–1699.
- (63) Levi, E.; Aurbach, D. Chevrel Phases, $M_xMo_6T_8$ ($M = \text{Metals}$, $T = S, Se, Te$) as a Structural Chameleon: Changes in the Rhombohedral Framework and Triclinic Distortion. *Chem. Mater.* **2010**, *22*, 3678–3692.
- (64) Smeu, M.; Hossain, M. S.; Wang, Z.; Timoshhevskii, V.; Bevan, K. H.; Zaghib, K. Theoretical investigation of Chevrel phase materials for cathodes accommodating Ca^{2+} ions. *J. Power Sources* **2016**, *306*, 431–436.
- (65) Juran, T. R.; Smeu, M. Hybrid density functional theory modeling of Ca, Zn, and Al ion batteries using the Chevrel phase Mo_6S_8 cathode. *Phys. Chem. Chem. Phys.* **2017**, *19*, 20684–20690.
- (66) Handbook, C. CRC Handbook of Chemistry and Physics, 88th ed.; CRC Press, 2007.

- (67) Carrasco, J. Role of van der Waals Forces in Thermodynamics and Kinetics of Layered Transition Metal Oxide Electrodes: Alkali and Alkaline-Earth Ion Insertion into V_2O_5 . *J. Phys. Chem. C* **2014**, *118*, 19599–19607.
- (68) Das, T.; Tosoni, S.; Pacchioni, G. Layered oxides as cathode materials for beyond-Li batteries: A computational study of Ca and Al intercalation in bulk V_2O_5 and MoO_3 . *Comput. Mater. Sci.* **2021**, *191*, No. 110324.
- (69) Tchitchevka, D. S.; Frontera, C.; Ponrouch, A.; Krich, C.; Bardé, F.; Palacín, M. R. Electrochemical calcium extraction from 1D- $Ca_3Co_2O_6$. *Dalton Trans.* **2018**, *47*, 11298–11302.
- (70) Hannah, D. C.; Gautam, G. S.; Canepa, P.; Rong, Z.; Ceder, G. Magnesium ion mobility in post-spinels accessible at ambient pressure. *Chem. Commun.* **2017**, *53*, 5171–5174.
- (71) Koettgen, J.; Bartel, C. J.; Shen, J.-X.; Persson, K. A.; Ceder, G. First-principles study of $CaB_{12}H_{12}$ as a potential solid-state conductor for Ca. *Phys. Chem. Chem. Phys.* **2020**, *22*, 27600–27604.
- (72) Zhang, Z.; Zhang, X.; Zhao, X.; Yao, S.; Chen, A.; Zhou, Z. Computational Screening of Layered Materials for Multivalent Ion Batteries. *ACS Omega* **2019**, *4*, 7822–7828.
- (73) Henkelman, G.; Jónsson, H. Improved tangent estimate in the nudged elastic band method for finding minimum energy paths and saddle points. *J. Chem. Phys.* **2000**, *113*, 9978–9985.
- (74) Martinolich, A. J.; Lee, C.-W.; Lu, I.-T.; Bevilacqua, S. C.; Preefer, M. B.; Bernardi, M.; Schleife, A.; See, K. A. Solid-State Divalent Ion Conduction in $ZnPS_3$. *Chem. Mater.* **2019**, *31*, 3652–3661.
- (75) Shannon, R. D. Revised effective ionic radii and systematic studies of interatomic distances in halides and chalcogenides. *Acta Crystallogr., Sect. A: Cryst. Phys., Diff., Theor. Gen. Crystallogr.* **1976**, *32*, 751–767.
- (76) Gautam, G. S.; Sun, X.; Duffort, V.; Nazar, L. F.; Ceder, G. Impact of intermediate sites on bulk diffusion barriers: Mg intercalation in $Mg_2Mo_3O_8$. *J. Mater. Chem. A* **2016**, *4*, 17643–17648.
- (77) Henkelman, G.; Uberuaga, B. P.; Jónsson, H. A climbing image nudged elastic band method for finding saddle points and minimum energy paths. *J. Chem. Phys.* **2000**, *113*, 9901–9904.
- (78) Perdew, J. P.; Burke, K.; Ernzerhof, M. Generalized Gradient Approximation Made Simple. *Phys. Rev. Lett.* **1996**, *77*, 3865–3868.
- (79) Kresse, G.; Furthmüller, J. Efficient iterative schemes for ab initio total-energy calculations using a plane-wave basis set. *Phys. Rev. B* **1996**, *54*, 11169–11186.
- (80) Kresse, G.; Furthmüller, J. Efficiency of ab-initio total energy calculations for metals and semiconductors using a plane-wave basis set. *Comput. Mater. Sci.* **1996**, *6*, 15–50.
- (81) Kresse, G.; Joubert, D. From ultrasoft pseudopotentials to the projector augmented-wave method. *Phys. Rev. B* **1999**, *59*, 1758–1775.
- (82) Wang, L.; Maxisch, T.; Ceder, G. Oxidation energies of transition metal oxides within the GGA+U framework. *Phys. Rev. B* **2006**, *73*, No. 195107.
- (83) Zhou, F.; Maxisch, T.; Ceder, G. Configurational Electronic Entropy and the Phase Diagram of Mixed-Valence Oxides: The Case of Li_xFePO_4 . *Phys. Rev. Lett.* **2006**, *97*, No. 155704.
- (84) Franchini, C.; Podloucky, R.; Paier, J.; Marsman, M.; Kresse, G. Ground-state properties of multivalent manganese oxides: Density functional and hybrid density functional calculations. *Phys. Rev. B* **2007**, *75*, No. 195128.
- (85) Hinuma, Y.; Meng, Y. S.; Ceder, G. Temperature-concentration phase diagram of $P2-Na_xCoO_2$ from first-principles calculations. *Phys. Rev. B* **2008**, *77*, No. 224111.
- (86) Jain, A.; Hautier, G.; Ong, S. P.; Moore, C. J.; Fischer, C. C.; Persson, K. A.; Ceder, G. Formation enthalpies by mixing GGA and GGA+U calculations. *Phys. Rev. B* **2011**, *84*, No. 045115.
- (87) Sai Gautam, G.; Carter, E. A. Evaluating transition metal oxides within DFT-SCAN and SCAN+U frameworks for solar thermochemical applications. *Phys. Rev. Mater.* **2018**, *2*, No. 095401.
- (88) Dudarev, S. L.; Botton, G. A.; Savrasov, S. Y.; Humphreys, C. J.; Sutton, A. P. Electron-energy-loss spectra and the structural stability of nickel oxide: An LSDA + U study. *Phys. Rev. B* **1998**, *57*, 1505–1509.
- (89) Sheppard, D.; Terrell, R.; Henkelman, G. Optimization methods for finding minimum energy paths. *J. Chem. Phys.* **2008**, *128*, No. 134106.